CIRP Journal of Manufacturing Science and Technology 51 (2024) 201–212

Contents lists available at ScienceDirect

CIRP Journal of Manufacturing Science and Technology

journal homepage: www.elsevier.com/locate/cirpj

Influence of spatial engagement angles on machining forces and surface roughness in turning of unidirectional CFRP

Alexander Brouschkin [*], Wolfgang Hintze, Jan Hendrik Dege

Institute of Production Management and Technology (IPMT), Hamburg University of Technology (TUHH), Denickestr. 17, 21073 Hamburg, Germany

ARTICLE INFO

Keywords:
Fibre reinforced plastics
Cutting
Turning
Spatial engagement conditions
Friction
Friction coefficient

ABSTRACT

Carbon fibre-reinforced polymer (CFRP) is being widely used due to its low specific weight and outstanding mechanical properties. However, using identical machining parameters on unidirectional CFRP can lead to different results depending on the fibre orientation.

Recently, a process-independent model describing the engagement conditions in oblique cutting of unidirectional CFRP has been developed, introducing the spatial angles θ_0 and φ_0. Since the engagement conditions of milling and drilling are complex, analogy experiments are conducted in turning with variation of the setting κ_r and inclination angles λ_s. In this study, process forces and surface roughness were measured as a function of the complete range of fibre cutting angle θ.

1. Introduction

Due to the increasing importance of energy and resource efficiency, there is a rising demand for lightweight components. These components are increasingly made from carbon fibre-reinforced plastics (CFRP). This trend is evident in the rising demand for carbon fibres [1], which serve as vital construction materials in the aerospace and automotive industry. The machining of CFRP plays a crucial role in the production process for shaping and assembling these lightweight components.

CFRP consists of two main components: carbon fibres and a polymer matrix. Carbon fibres demonstrate exceptional mechanical properties when subjected to forces aligned with their fibre orientation. However, they are prone to bending or buckling when forces are applied perpendicular or opposite to their orientation and are incapable of independently withstanding mechanical loads. On the other hand, the polymer matrix is an isotropic material with lower mechanical properties. By embedding the fibres the matrix offers support against transverse loads, and protects them from environmental influences. The matrix can be composed of thermoset or thermoplastic polymers [2].

As a consequence of the combination of properties of its two main components, CFRP demonstrates a dependence of its mechanical attributes on the fibre orientation. These anisotropic characteristics facilitate an optimization of the lightweight component in the direction of stress. However, machining unidirectional CFRP is challenging due to its anisotropic behavior, resulting in variable process forces and surface quality under identical machining parameters with different fibre orientations. This is illustrated in Fig. 1 using an example of a countersinking process of unidirectional CFRP. The fibre cutting angle θ which is positively enclosed between the cutting speed vector and the fibre direction characterizes this dependency [4–7]. In the region around $\theta = 45^\circ$, a rough, stepped surface is evident, clearly distinguishing itself from the smooth cutting surface at lower fibre cutting angles θ.

Due to the anisotropy and orthotropy of the CFRP, the description of the spatial engagement conditions between cutting edge and fibre is important. In the first step, Hintze et al. [6] developed a description of the engagement conditions in the laminate plane. Thereby, the fibre cutting angle θ, positively enclosed between the cutting speed vector and the fibre direction as well as the fibre orientation angle Φ, positively enclosed between the feed vector and the fibre direction were introduced.

Previous work has shown that the cutting force components (F_c, F_f, F_p) behave π-periodically with θ. In the range $30^\circ < \theta < 60^\circ$, the forces pass through a minimum. While F_f and F_p reach a maximum between $120^\circ < \theta < 180^\circ$, the cutting force reaches it at about $\theta = 90^\circ$ [4–7]. Likewise, optical examinations of the machined surface revealed material defects, such as fibre pull-out and delamination during drilling, which can be attributed to the engagement conditions of the tool with respect to the fibre direction [8,9]. For example, the measured roughness of the machined surfaces (Ra, Rz, Rt) reaches a significant maximum in the range $30^\circ < \theta < 60^\circ$, while for all other angles it is

---

[*] Corresponding author.
E-mail address: alexander.brouschkin@tuhh.de (A. Brouschkin).

https://doi.org/10.1016/j.cirpj.2024.03.010
Received 20 October 2023; Received in revised form 15 February 2024; Accepted 26 March 2024

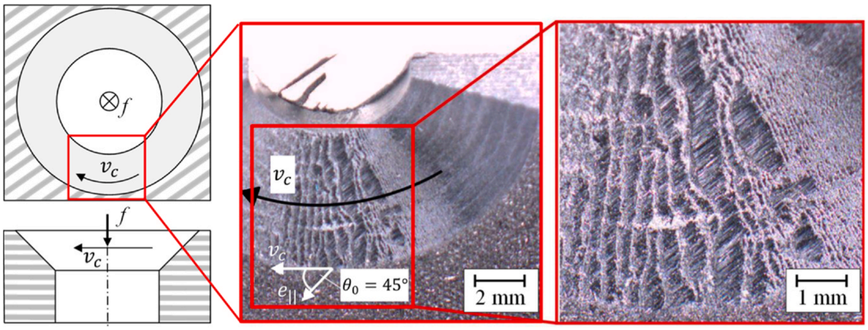

Fig. 1. Fibre break-out by different fibre cutting angles during countersinking [3].

constant at Rz < d_f. As shown in Fig. 1 at $\theta = 45°$ a fibre-break-out occurs resulting in high surface roughness, low machining forces and deep cracks in the laminate [3]. This phenomenon of fibre-break-out occurs due to a tool-pull-in [11] and will be referred to as tool-pull-in effect in this work.

Nomenclature

CFRP	Carbon fibre reinforced polymer	e_p	Normal vector to the tool back plane
WC-CO	Cemented carbide	P_s	Cutting plane
DC	Diamond coated	φ	Engagement angle [°]
f_{lp}	Low-Pass-Filter Frequency [Hz]	θ	Fibre cutting angle [°]
l_n	Measurement length [mm]	θ_0	Spatial fibre cutting angle [°]
λ_c	Cut-Off wave length roughness measurements [mm]	φ_0	Spatial engagement angle [°]
α_e	Effective clearance angle [°]	v_c	Cutting speed [m/min]
γ_e	Effective rake angle [°]	f	Feed [mm/min]
α_f	Tool clearance angle [°]	a_p	Depth of cut [mm]
γ_f	Tool rake angle [°]	h	Undeformed chip thickness [mm]
ψ	Angular deviation due to tool inclination [°]	b	Width of undeformed chip thickness [mm]
κ_r	Setting angle [°]	b_λ	Cutting edge engagement length [mm]
σ_r	Drill point angle $2 \cdot \kappa_r$ [°]	r_β	Cutting edge radius [μm]
ρ	Tilt angle [°]	F_z	Resultant force [N]
λ_s	Inclination angle of the cutting edge [°]	F_c	Cutting force [N]
λ_t	Helix angle of the milling tool [°]	F_f	Feed force [N]
λ_v	Inclination of the milling tool [°]	F_p	Passive force [N]
χ,ξ,ν,ζ	Transformation angles [°]	$F_{\kappa t}$	Force perpendicular to v_c [N]
$e_{\|\|}$	Unit vector in fibre direction	$F_{\kappa n}$	Force perpendicular to the cutting plane [N]
$e_{\perp 1}$	Unit vector in laminate direction	μ	Friction coefficient
$e_{\perp 2}$	Unit vector in laminate thickness direction	μ	Indices: Friction component
e_r	Normal vector to the tool reference plane	s	Indices: Separation component
e_s	Normal vector to the cutting plane	Ra	Linear mean roughness [μm]
e_o	Normal vector to the orthogonal plane	Rz	Mean roughness depth [μm]
e_f	Normal vector to the working plane	Rt	Maximum peak valley to height [μm]
		d_f	Fibre diameter [μm]
		D	Bore diameter [mm]

(continued on next column)

(continued)

Different separation mechanisms occur at different θ. At $\theta = 0°$, mainly the matrix is separated, resulting in peeling and kinking of fibres at the cutting edge. At $\theta = 45°$, the fibres are strongly bent and separated in packages. Furthermore, cracks appear which lead into the laminate. This results in a tool-pull-in effect which leads to high surface roughness and low machining forces [11]. At $\theta = 90°$, the fibres are bent and separated individually. At $\theta = 135°$, the fibres are separated in fibre matrix packets due to interfacial failure in thermosets such as epoxy resin. [10].

Based on the orthotropy of the fibres, Hintze et al. developed a novel, process-independent description of the engagement conditions during the machining of CFRP. With the position of the cutting plane and the spatial position of the cutting speed vector in relation to the fibre orientation, Hintze defined the spatial engagement angles θ_0 and ϕ_0. This allows different engagement conditions of different machining processes to be shown and compared with each other. [11].

When machining CFRP, a coefficient of friction independent of θ has been assumed [12]. The dependence of the coefficient of friction on θ was investigated by Sung and Voss. Using a friction test setup Sung found a slight increase in the coefficient of friction from $\mu = 0.25 - 0.6$ for the range $90° < \theta < 180°$ [13] whereas Voss et al. measured $\mu = 0.12 - 0.14$ [17] in orthogonal turning for the range $0° < \theta < 180°$.

The engagement conditions in typical CFRP machining processes, such as milling and drilling, are complex, which poses significant challenges for fundamental investigations. In milling, the undeformed chip thickness h varies along the engagement, and in drilling, a changing inclination angle λ_s occurs due to the chisel edge. In other machining processes like planing, only one fibre cutting angle can be examined at a time.

Turning experiments are used to investigate fundamental relationships between spatial engagement conditions and process forces and surface roughness. This approach enables the investigation of the entire range of θ while maintaining mostly constant machining parameters, such as the undeformed chip thickness h and a mostly consistent cutting-

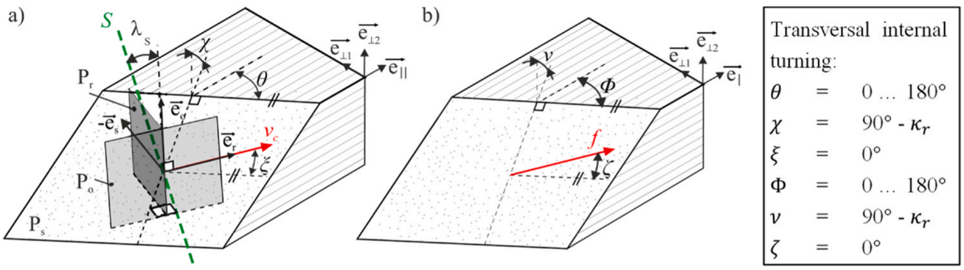

Fig. 2. Description of cutting (a) and feed direction (b) in oblique cut of orthotropic materials [according to 11].

Table 1
Feed rate for different settling angles by constant undeformed chip width.

κ_r	f	h
90°	0.040 mm	0.040 mm
75°	0.041 mm	
60°	0.046 mm	
45°	0.056 mm	
30°	0.080 mm	

edge geometry. The experiments are used to validate the process-independent model proposed by Hintze et al. [11], which was initially based on the evaluation of available data from literature and small inclination angles of the cutting edge. Furthermore, process-independent machining force components are introduced into the model as well as the decomposition of the machining force into friction and separation forces. Thereby, the foundation for a cross-process modelling of the complex engagement conditions in more common machining processes as milling is achieved.

2. Model of the engagement conditions

2.1. Description of engagement conditions

Based on the angles θ and Φ, Hintze et al. developed a description of the spatial engagement conditions during the oblique cut of FRP with reference angles, in which they applied a transformation of the workpiece coordinate system $\{\overrightarrow{e_{||}}, \overrightarrow{e_{\perp 1}}, \overrightarrow{e_{\perp 2}}\}$ into the tool coordinate system $\{\overrightarrow{e_r}, \overrightarrow{e_s}, \overrightarrow{e_o}\}$ (Fig. 2) [11,14]. In the process, further angles necessary for the transformation are introduced:

$$\begin{pmatrix} \overrightarrow{e_{||}} \\ \overrightarrow{e_{\perp 1}} \\ \overrightarrow{e_{\perp 2}} \end{pmatrix} = \begin{bmatrix} \cos\theta & \sin\theta & 0 \\ -\sin\theta & \cos\theta & 0 \\ 0 & 0 & 1 \end{bmatrix} \bullet \begin{bmatrix} 1 & 0 & 0 \\ 0 & \cos\chi & \sin\chi \\ 0 & -\sin\chi & \cos\chi \end{bmatrix} \bullet \begin{bmatrix} \cos\xi & 0 & -\sin\xi \\ 0 & 1 & 0 \\ \sin\xi & 0 & \cos\xi \end{bmatrix} \cdot \begin{pmatrix} \overrightarrow{e_r} \\ \overrightarrow{e_s} \\ \overrightarrow{e_o} \end{pmatrix} \quad (1)$$

For a complete description of the engagement conditions, the inclination angle λ_s describes the inclination angle of the cutting edge in the cutting plane P_s. Table 1 shows typical values for the newly introduced angles in the various cutting processes, where φ represents the engagement angle of the cutting edge in the workpiece material during rotary cutting processes.

Taking into account the orthotropy of the material, Hintze et al. [11] introduce the spatial engagement angles, which describe the spatial angles between the vectors $-\overrightarrow{e_s}$ and $\overrightarrow{e_{||}}$ for the spatial fibre cutting angle θ_0 and between the vectors $\overrightarrow{e_r}$ and $\overrightarrow{e_{||}}$ for the spatial engagement angle ϕ_0, as shown in Fig. 3a). This results in the following relationships between the spatial angles:

$$\cos(\theta_0) = \langle e_r, e_{||} \rangle \quad (2)$$

$$\cos(\varphi_0) = \langle e_s, e_{||} \rangle \quad (3)$$

$$0^\circ \le \varphi_0 \le 90^\circ \quad (4)$$

$$90^\circ - \varphi_0 \le \theta_0 \le 90^\circ + \varphi_0 \quad (5)$$

The spatial engagement angles can be calculated from the reference angles for machining operations, whereby the spatial engagement conditions can be described independently of the machining process. Fig. 3b shows the relationship between the spatial angles θ_0 and φ_0 for different machining processes. Based on the definitions (Eqs. 3, 4), a triangle results in the θ_0-φ_0-plane for the area of definition. The influence of the inclination angle cannot be depicted with this diagram. Using the description of the spatial engagement conditions, Hintze et al. found a correlation between the cutting forces and the surface roughness for different cutting processes with low inclination angle ($\lambda_s < 15^\circ$). Regardless of the individual cutting process, minimum forces occurred in the range of $40^\circ < \theta_0 < 60^\circ$ and $65^\circ < \varphi_0 < 75^\circ$, maximum forces at $140^\circ < \theta_0 < 160^\circ$ and $55^\circ < \varphi_0 < 65^\circ$ and maximum roughness Rz in the range $45^\circ < \theta_0 < 75^\circ$ and $45^\circ < \varphi_0 < 75^\circ$. From this, Hintze et al. concluded that low or negative feed forces lead to an increase in surface roughness. This can be explained by a tool pull-in and the resulting fibre break-outs [11]. In this paper, different spatial engagement conditions in transverse internal turning of CFRP and the variation of inclination and setting angle (λ_s, κ_r) are investigated.

A constraint for using this description is that the same or similar measured values occur under the same engagement conditions. All processes shown pass $\theta_0 = 0^\circ$ or 180° and $\varphi_0 = 90^\circ$, which corresponds to the point $\theta = 0^\circ$ or 180° regardless of other process angles such as the setting angle κ_r, lead or tilt angle. If the measured values do not fulfil the constraint, they must be broken down into components that fulfil it. Otherwise, the applicability of the θ_0,ϕ_0-description must be questioned.

2.2. Adapting the forces to the spatial engagement angles

Next, the force decomposition is adapted to the model of the spatial engagement angles. A suitable division of the resultant force is the following: a force in the direction of the cutting speed $\overrightarrow{e_r}$ as force component F_c, a force in the direction of the unit vector $\overrightarrow{e_s}$ orthogonal to the cutting plane as force component $F_{\kappa n}$ and a force perpendicular to v_c in direction of $\overrightarrow{e_o}$ as force component $F_{\kappa t}$. The transformation of the force components $\{F_c, F_f, F_p\}$ from the coordinate system $\{\overrightarrow{e_r}, \overrightarrow{e_f}, \overrightarrow{e_p}\}$ to the force components $\{F_c, F_{\kappa n}, F_{\kappa t}\}$ in the tool coordinate system $\{\overrightarrow{e_r}, \overrightarrow{e_s}, \overrightarrow{e_o}\}$ proceeds as follows:

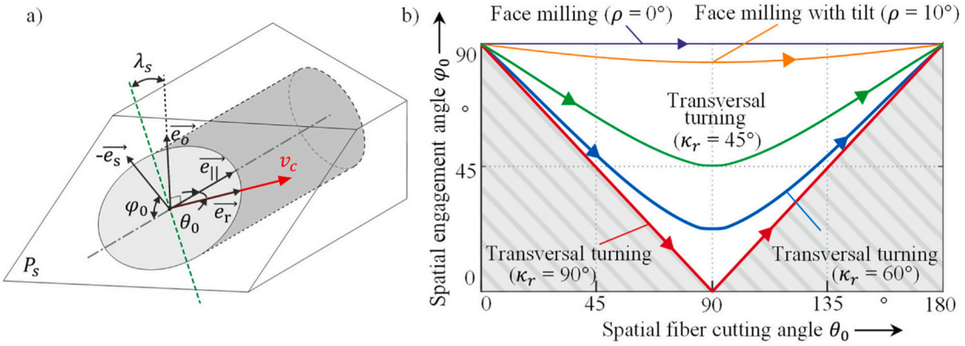

Fig. 3. a) Description of cutting direction with spatial engagement angles θ_0, φ_0; b) θ_0, φ_0- diagram for common cutting operations. [according to 11].

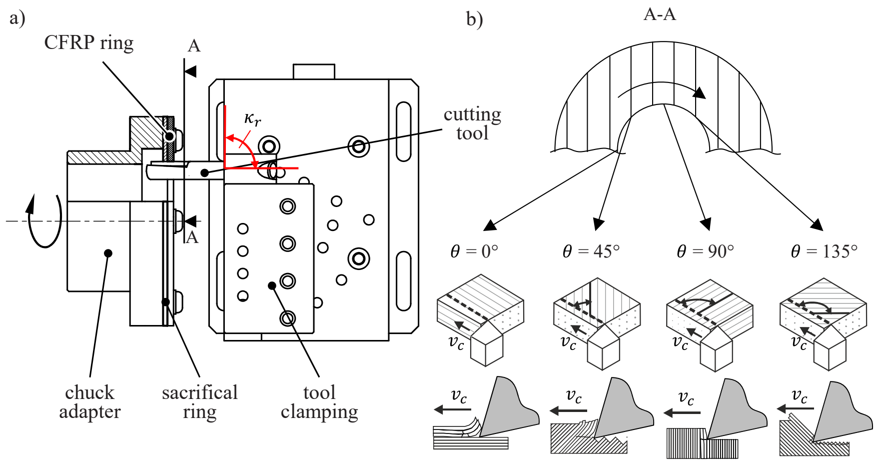

Fig. 4. a) Experimental set up; b) Fibre cutting angle during transverse internal turning by $\lambda_s = 0°$ and $\kappa_r = 90°$.

$$\begin{pmatrix} \overrightarrow{F_c} \\ \overrightarrow{F_{\kappa n}} \\ \overrightarrow{F_{\kappa t}} \end{pmatrix} = \begin{pmatrix} 1 & 0 & 0 \\ 0 & \sin(\kappa_r) & \cos(\kappa_r) \\ 0 & -\cos(\kappa_r) & \sin(\kappa_r) \end{pmatrix} \cdot \begin{pmatrix} \overrightarrow{F_c} \\ \overrightarrow{F_f} \\ \overrightarrow{F_p} \end{pmatrix} \tag{6}$$

This force decomposition has the advantage that $F_{\kappa n}$, as a force always orthogonal to the cutting plane Ps, is both the perpendicular component of the friction force and the force component essential for the formation of the surface. The force components $F_{\kappa t}$ and F_c, which lie in the cutting plane Ps, are the force components required to separate the fibre. Furthermore F_c forms the tangential component of the friction force. In accordance with the description of the engagement conditions with two spatial angles, two force components are also considered in this work: the force sum $\overrightarrow{F_c} + \overrightarrow{F_{\kappa t}}$ and $F_{\kappa n}$.

The resultant force F_z can be further decomposed into the friction force $F_{z,\mu}$ and the separation force $F_{z,s}$.

$$F_{z,s} = F_z - F_{z,\mu} \tag{7}$$

Where $F_{z,\mu}$ depends on the engagement conditions and the cutting-edge length in engagement b_λ and can thus be scaled via b_λ. $F_{z,s}$ depends on the engagement conditions and on the number of fibres cut, but not on b_λ. There is no relationship between b_λ and the number of separated fibres when the depth of cut a_p is constant, since changing κ_r changes b_λ but the number of separated fibres remains constant. b_λ is calculated as follows:

$$b_\lambda = a_p \cdot \frac{1}{\sin(\kappa_r)} \cdot \frac{1}{\cos(\lambda_s)} \tag{8}$$

3. Experimental setup

3.1. Machining tests

The experiments are carried out in transverse internal turning. A cemented carbide endmill (grade CERATIZIT CTS12D) with a Oerlikon BALDIA® COMPOSITE DC diamond coating (thickness of 12 +3 μm) is used as cutting tool and a CFRP ring with a thickness of d = 4 mm made out of unidirectional CFRP (HexPly 6376, HTS 12k) is turned outwards through a previously made bore hole (D = 70 mm).

To realise different spatial engagement conditions, the setting angle κ_r, the fibre cutting angle θ and the inclination angle λ_s are varied. θ changes from 0° to 180° due to the rotation of the workpiece twice per revolution as shown in Fig. 4b. The inclination and setting angle increments were defined in a way that they cover the ranges of λ_s and κ_r of typical CFRP machining processes as milling, drilling or sawing and according tools. Hereby, λ_s is varied in three steps $\lambda_s = 0°$, $\lambda_s = 15°$, $\lambda_s = 30°$. As a further influencing factor, the undeformed chip thickness h is hold constant at $h = 40$ μm. Therefore, the feed rate f increases with decreasing κ_r as shown in Table 1.

Fig. 4 shows the experimental setup with the tool holder mounted on a dynamometer (Kistler 9257B). Fig. 4a shows the change of the setting angle κ_r, which is varied from $\kappa_r = 90°$ in 15° steps to $\kappa_r = 30°$. The

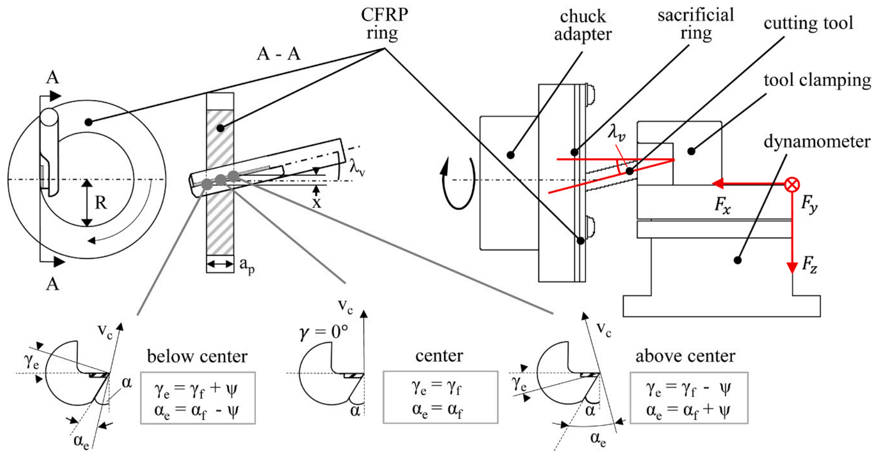

Fig. 5. Change of the inclination angle λ_s in the experimental setup and change of rake and clearance angles when changing the angle of inclination.

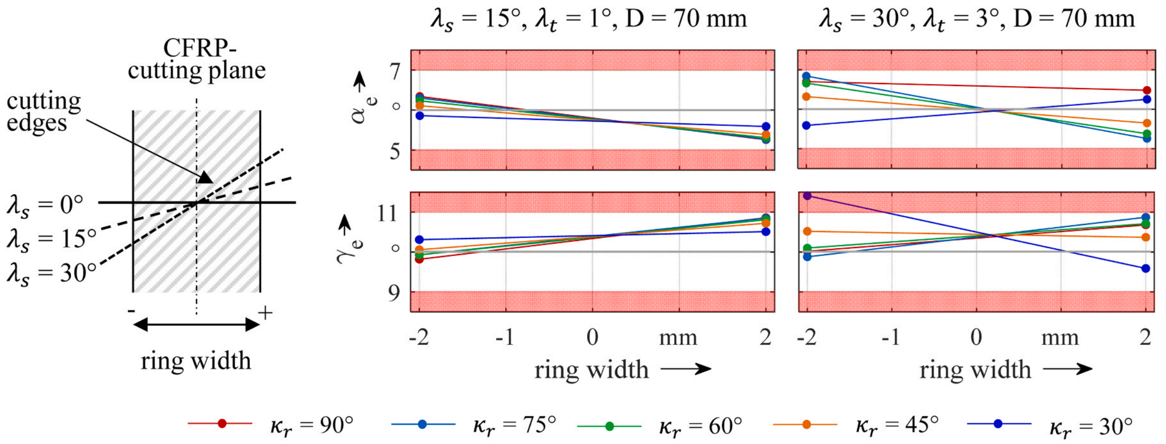

Fig. 6. Change of α_e and γ_e as a function of the CFRP-ring width.

selection of angular increments for λ_s and κ_r was based on the following rationale: Initially, it was unclear how the combination of inclination and setting angles would impact the positioning of extreme values for forces and surface roughness in the θ_0-φ_0-diagramm. With the perspective of decreasing angular increments leading to a disproportionately increasing experimental effort, a compromise of a 15° angular increment was selected.

When λ_s is varied α_e and γ_e change at $\lambda_s \neq 0°$ across the width of the ring due to the over- and under-centre position of the cutting edge. For the tests, a maximum change of ±1° in the rake and clearance angles over the entire width of the ring was accepted. For the deviation ψ applies:

$$\psi = \arctan\left(\frac{x}{R}\right) \tag{9}$$

$$\mathrm{x} = \mathrm{a_p} \bullet \tan(\lambda_\mathrm{v}) \tag{10}$$

To compensate for the deviation, endmills with a slight helix angle λ_t were chosen, so that the following applies:

$$\lambda_s = \lambda_t + \lambda_v \tag{11}$$

Fig. 5 shows the relationship between the effective rake and clearance angles (γ_e, α_e) as the inclination angle.

The variation of λ_v is shown in Fig. 5. For each λ_s a separate endmill is employed as the helix angle of the milling tool λ_t is used to compensate the angular deviation due to the tool inclination ψ. For an inclination angle $\lambda_s = 0°$ a $\lambda_t = 0°$ is used. For an inclination angle $\lambda_s = 15°$ a $\lambda_t = 1°$ is used and for $\lambda_s = 30°$ a $\lambda_t = 3°$ is used. Thus, the set condition for α_e and γ_e can be fulfilled for the bore diameters D = 70 - 100 mm as shown in Fig. 6. Except for the combination $\lambda_s = 30°$ and $\kappa_r = 30°$, the condition is fulfilled for all λ_s-κ_r combinations. Higher λ_s cannot be realized with this test setup due to the change in effective clearance and rake angle as well as the fibre cutting angle θ_0, so constant engagement conditions cannot be ensured.

Throughout the machining experiments, the cutting-edge radius of the endmill at $\lambda_s = 0°$ exhibited a notable increase due to tool wear, growing from an initial value of $r_\beta = 22$ µm to $r_\beta = 35$ µm. Similarly, for the endmill at $\lambda_s = 15°$, the cutting-edge radius expanded from $r_\beta = 19$ µm to $r_\beta = 28$ µm, while for the endmill at $\lambda_s = 30°$, the radius experienced a smaller increment, rising from $r_\beta = 18$ µm to $r_\beta = 20$ µm. Repeated experiments with different cutting-edge radii r_β showed no influence of the cutting-edge radius r_β on the roughness parameters. However, the influence of the increasing r_β on the process forces was accounted for by a force correction factor (Section 4.2).

To avoid delamination and deformation of the CFRP ring, a sacrificial ring out of aluminium (thickness d = 3 mm) is clamped between the chuck adapter and the CFRP ring. This supports the CFRP ring at low κ_r and thus prevents delamination.

To determine the fibre cutting angle during the process, the angular position of the spindle is recorded. For this purpose, a mark on a dedicated fibre cutting angle θ is placed on the spindle, which passes a displacement sensor. This sensor signal is recorded isochronous to the force data. The measured forces can be converted into the cutting force components by means of Fig. 4a and the following equations:

$$F_c = F_z \tag{12}$$

$$F_f = -F_y \tag{13}$$

$$F_p = -F_x \tag{14}$$

For the evaluation, the mean value of the last 5 π-periods of the fibre cutting angle is calculated for each cutting force component. The force signal is filtered with a low-pass filter with a frequency of $f_{lp} = 300$ Hz.

3.2. *Transformation of fibre cutting and setting angles to spatial engagement angles*

According to Fig. 2 and the Eqs. (1, 2, 3) the following calculation can be made for the spatial engagement angles for transverse internal turning as a function of the fibre separation angle θ and the setting angle κ_r:

$$\theta_0 = \theta \tag{15}$$

$$\varphi_0 = \arccos(\sin(\theta)\cdot\cos(90° - \kappa_r)) \tag{16}$$

For the representation of the results in the θ_0-φ_0-plane, the average values of single measurements at each measured θ_0-φ_0- combination is interpolated linearly. R^2 indicates accordingly the deviation of the single measurements at each measured θ_0-φ_0- combination.

3.3. *Roughness measurement*

The machining experiments are used both to determine the cutting forces and the surface roughness. In order to eliminate the influence of the chip thickness on the roughness, the cutting edge must be withdrawn from the cut in a maximum time corresponding to half a revolution, so that one half of the bore surface is not machined with a lower chip thickness that occurs when the cutting edge is withdrawn from the cut. For this a reverse feed of 5000 mm/min is sufficient. No indication of the withdrawal of the cutting edge could be detected on the cut surface. Assuming that one half of the ring has lower *h,* the whole surface was measured so two measurements for each θ_0 were obtained. The deviation between these two measurements was in range of the standard deviation if only the highest measured value for each θ were used.

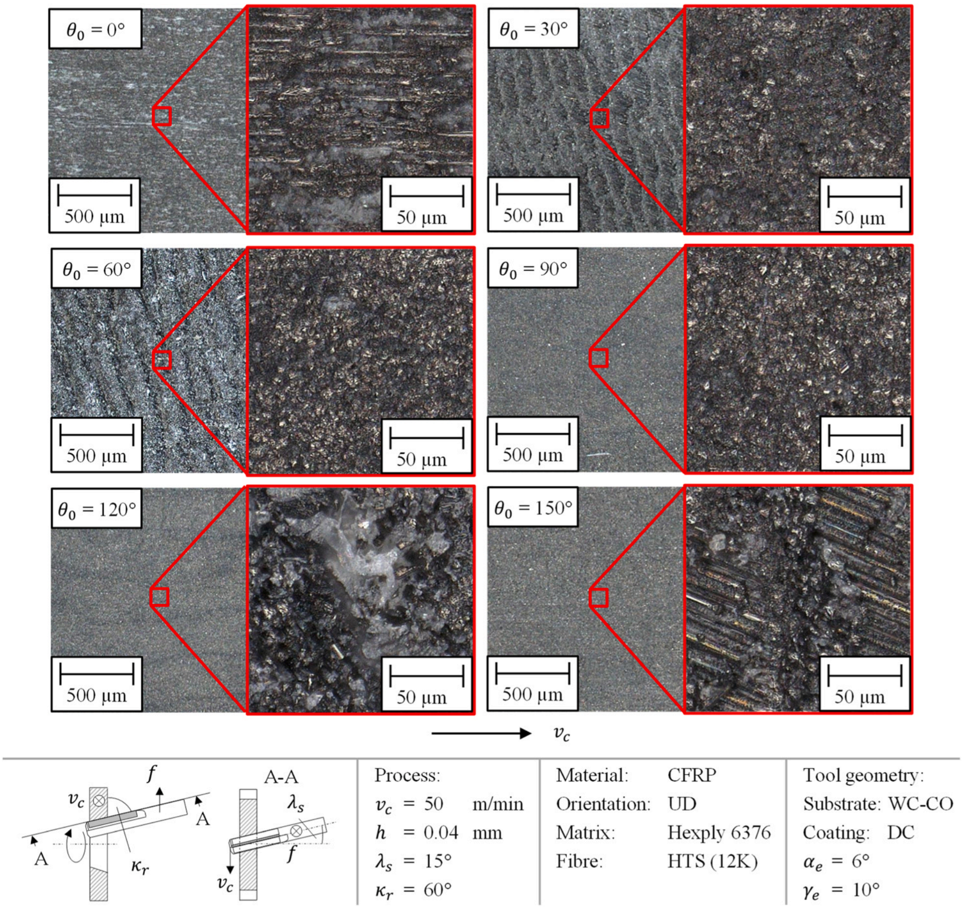

Fig. 7. Machined surface at different θ_0 for constant tool settings of $\kappa_r = 60°$ and $\lambda_s = 15°$.

A tactile roughness instrument is used to measure the line roughness. Here, the roughness is measured parallel to the cutting speed direction at a constant fibre cutting angle 1 mm apart from each edge of the laminate. Roughness values are recorded for $\theta = 0 - 180°$ in 15° increments, with an average of 4 measurements obtained at each θ. The measurement settings are $l_n = 5.6$ mm and $\lambda_c = 0.8$ mm. For the presentation of the results the roughness parameter Rz was chosen because it introduces stochasticity compared to Rt and highlights the height of the steps compared to Ra.

3.4. Machining experiments

In the machining experiments, the stack of CFRP and aluminium sacrificial ring as well as the sacrificial ring alone are machined for 20 revolutions at a constant feed rate and then the cutting edge is withdrawn from the cut at $v_f = 5000$ mm/min. To evaluate the force signal, the cutting forces for the machining of the aluminium sacrificial ring were measured in advance. These are subtracted from the cutting forces measured during the machining of the CFRP-aluminium sacrificial ring stack.

3.5. Friction experiments

Friction experiments are carried out in order to decompose the force resulting from friction and that one resulting from material separation. The stack of CFRP and aluminium sacrificial ring and the sacrificial ring alone are machined for 10 revolutions with constant feed and then the position is held for 20 s without feed so that a stable signal for the

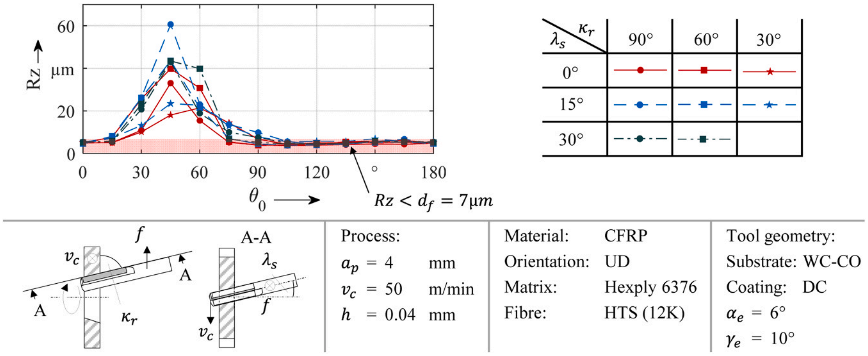

Fig. 8. Roughness as a function of θ_0.

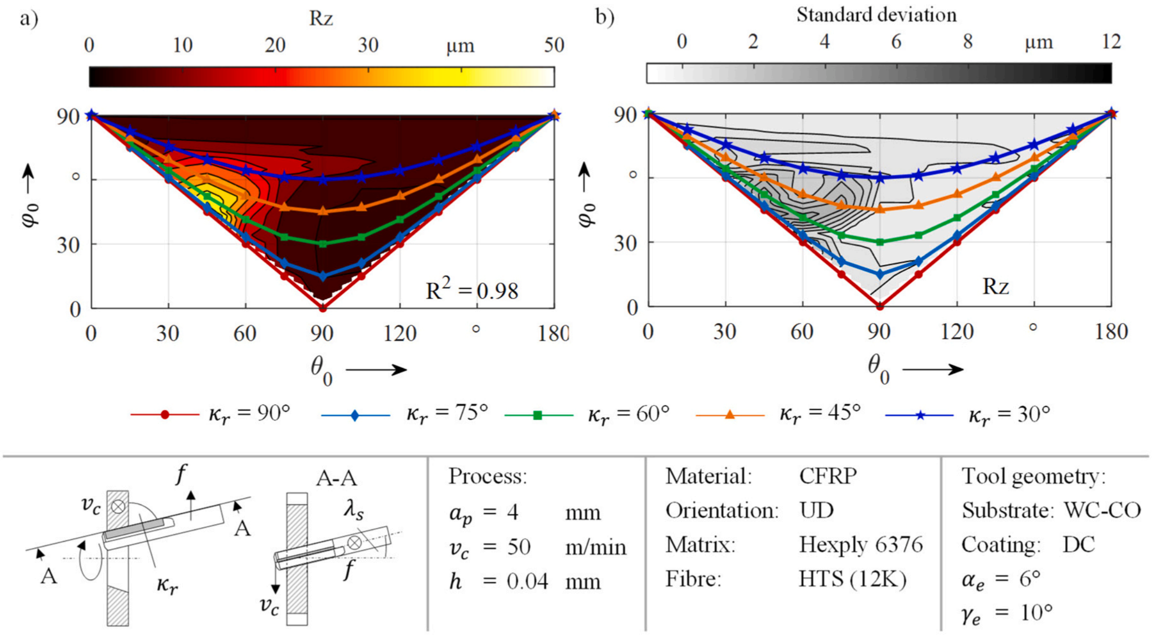

Fig. 9. Roughness in the θ_0-ϕ_0-plane for the measurement direction perpendicular and parallel to the cutting velocity direction.

friction force is established. To determine the friction forces of the CFRP, the friction forces of the sacrificial ring are subtracted from the forces of the stack. To determine the coefficient of friction, the force $F_{c,\mu}$ acting tangentially to the cutting velocity vector is divided by the force $F_{\kappa n,\mu}$ exerted perpendicular to both the cutting surface and the cutting velocity vector.

4. Experimental results

4.1. Surface roughness

Fig. 7 shows the cutting surface at different θ_0 for constant tool settings of $\kappa_r = 60°$ and $\lambda_s = 15°$. At $\theta_0 = 30°$ and $\theta_0 = 60°$, a stepped

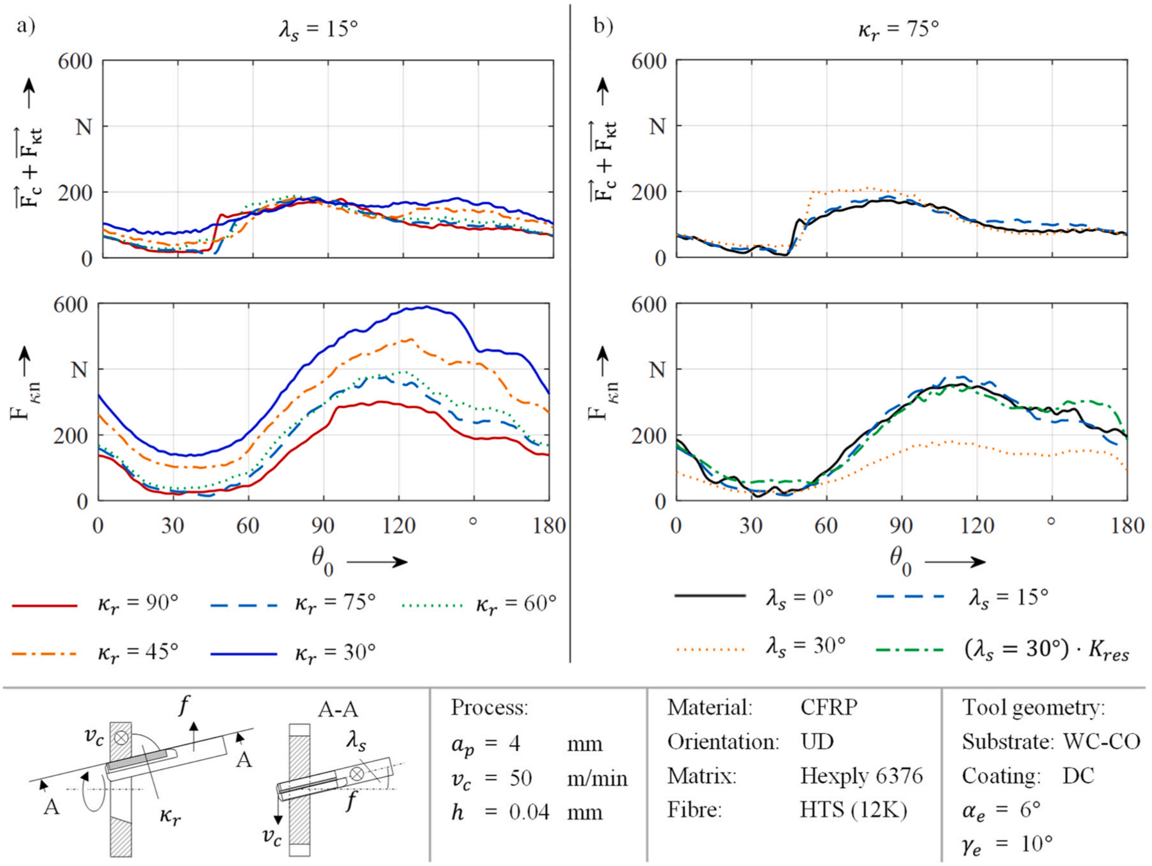

Fig. 10. Process forces as a function of a) setting angle κ_r, b) inclination angle λ_s.

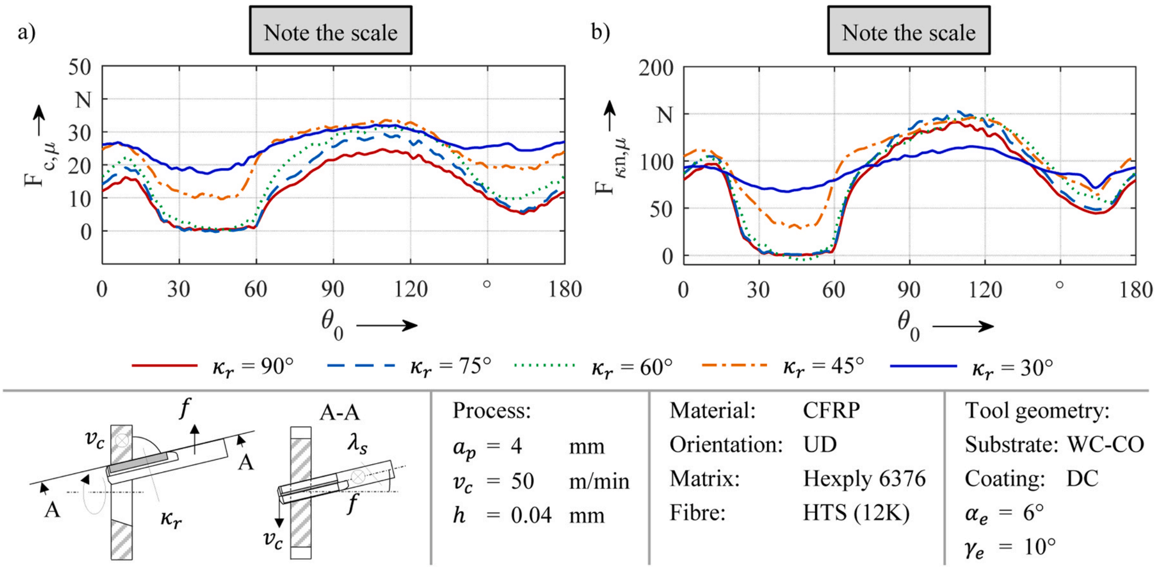

Process:
$a_p = 4$ mm
$v_c = 50$ m/min
$h = 0.04$ mm

Material: CFRP
Orientation: UD
Matrix: Hexply 6376
Fibre: HTS (12K)

Tool geometry:
Substrate: WC-CO
Coating: DC
$\alpha_e = 6°$
$\gamma_e = 10°$

Fig. 11. Friction forces normalised to $b_\lambda = 4$ mm as function of θ_0 a) $F_{c,\mu}$ for $\lambda_s = 15°$ b) $F_{\kappa n,\mu}$ for $\lambda_s = 15°$.

surface can be seen in the macroscopic image, which is an indication for the tool pull-in effect and goes along with high surface roughness. Smooth surfaces with distinct characteristics specific to the fibre cutting angle can be observed for other values of θ_0. For example, at $\theta_0 = 0°$, the fibre direction is visible as the fibres are peeled off layer by layer. At $\theta_0 = 90°$, individual separated fibres can be seen due to reflections. At $\theta_0 = 120°$ resin agglomerates between the individual fibre rovings can be observed. Such a matrix residue is visible on the microscopic image. At $\theta_0 = 150°$, fibre matrix bundles break-offs can be seen in the microscopic image, which creates a stepped surface with peaks up to 3 µm in height. This is common for thermoset matrices at this θ_0 [10].

Fig. 8 shows the roughness Rz as function of θ_0 for different combinations of κ_r and λ_s. With decreasing κ_r the roughness Rz decreases as well, though for $15° < \theta_0 < 90°$ Rz is significantly higher than the fibre diameter $d_f = 7$ µm. In the investigated angular range of λ_s the influence is of minor importance compared to θ_0 and κ_r.

Fig. 9a shows the development of Rz for $0 \leq \lambda_s \leq 30°$ in the θ_0-φ_0-plane and thus for different engagement conditions. The increase of Rz in the range $15° < \theta < 90°$ is reflected here in a maximum in the range $30° < \theta_0 < 75°$ and $30° < \varphi_0 < 15$. For other engagement conditions, a low roughness value of Rz = 6 - 12 µm is observed which lies in the range of the fibre diameter $d_f = 7$ µm. The clear boundary of the region of high roughness is noteworthy, as it does not occur at $\theta_0 > 75°$ and $\phi_0 < 30°$. One explanation of the high roughness is a possible tool-pull-in effect, which makes the cutting process unstable, leads to large vibrations and poor surface finish. Hintze et al. [11] showed similar behaviour of roughness in the θ_0-φ_0-plane. Fig. 9b shows the standard deviation of the roughness measurement. Areas with high surface roughness yields high variation of the measured values.

4.2. Process forces

Fig. 10 shows the sum of forces $\overrightarrow{F_c}+\overrightarrow{F_{\kappa t}}$ and $F_{\kappa n}$ as a function of θ_0, κ_r and λ_s. $\overrightarrow{F_c}+\overrightarrow{F_{\kappa t}}$ and $F_{\kappa n}$ are used for the representation as these force components lie inside the cutting plane P_s ($\overrightarrow{F_c}+\overrightarrow{F_{\kappa t}}$) or are perpendicular to P_s ($F_{\kappa n}$). As the spatial description of the engagement conditions considers the spatial orientation of the cutting plane (φ_0) and the cutting velocity direction in the cutting plane (θ_0) in respect to the fibre direction these force components are suitable for the θ_0-φ_0-description of the engagement conditions.

However, due to mechanical constraints of the experimental setup for the realization of high inclination angles, the clearance angle became negative which resulted in significant friction forces at $\lambda_s = 30°$, leading to increased feed and passive forces. Hence the endmill was rotated by 10°, resulting in an effective clearance angle $\alpha_e = 16°$ and an effective rake angle $\gamma_e = 0°$. Due to this change in the effective cutting tool geometry, the friction tests for $\lambda_s = 30°$ cannot be directly compared with the others. To ensure comparability of $F_{\kappa n}$ at $\lambda_s = 30°$, a force correction factor was experimentally determined.

As shown by Voss [6] the rake angle γ_e has a negligible effect on the cutting force F_c, feed force F_f and passive force F_p. Whereas an increasing effective clearance angle α_e leads to lower F_f and F_p and therefore to a lower $F_{\kappa n}$ and has no significant effect on the cutting forces F_c. Experiments showed an increase in $F_{\kappa n}$ by a factor of $K_\alpha = 1.25$ by changing the clearance angle from $\alpha_e = 14°$ to $\alpha_e = 6°$. However, the slightly higher wear of the endmills at $\lambda_s = 0°$ and $\lambda_s = 15°$ in comparison to $\lambda_s = 30°$ leads to higher $F_{\kappa n}$. A force correction factor for the wear, $K_r = 1.67$, was determined. The cumulated effect of tool wear K_r and change of the effective clearance angle $(\alpha_e)K_\alpha$ can be assumed as $K_{res} = K_\alpha \cdot K_r \approx 2$.

Fig. 10a shows the sum of forces $\overrightarrow{F_c}+\overrightarrow{F_{\kappa t}}$ and $F_{\kappa n}$ as a function of θ_0 and κ_r.The development of $\overrightarrow{F_c}+\overrightarrow{F_{\kappa t}}$ over θ_0 stays nearly the same over changing κ_r whereas $F_{\kappa n}$ increases with decreasing κ_r. This can be a result of the increasing width of undeformed chip b which leads in higher friction. Schütte [3] determined similar force developments over θ for F_c and F_f in his planing and countersinking experiments. By using similar engagement conditions in planing tests, Schütte obtained similar force values. The force minimum around $\theta \approx 45°$ is due to the described tool-pull-in effect.

Fig. 10b shows the resultant force components as a function of λ_s at $\kappa_r = 75°$. The force development over θ_0 of the forces in the cutting plane P_s ($\overrightarrow{F_c} + \overrightarrow{F_{\kappa t}}$) (Fig. 10b) show almost identical profiles, so that the statement can be made that λ_s has no significant influence on the force sum $\overrightarrow{F_c}+\overrightarrow{F_{\kappa t}}$ in the investigated range. In order to compensate the influence of the change in the effective cutting-edge geometry and slightly lower tool wear on $F_{\kappa n}$, $F_{\kappa n}$ for $\lambda_s = 30°$ were multiplied by the factor $K_{res} = 2$. The corrected force profile of $\lambda_s = 30°$ and the other inclination angles are almost congruent, so that $F_{\kappa n}$ is independent of λ_s, as is the force sum $\overrightarrow{F_c} + \overrightarrow{F_{\kappa t}}$. Since the force of individual κ_r do not have equal values at $\theta = 0°$ and $\theta_0 = 180°$, respectively, the constraint for θ_0-φ_0-description of the engagement conditions is not fulfilled. For further analysis, the process forces were divided into friction and separation components.

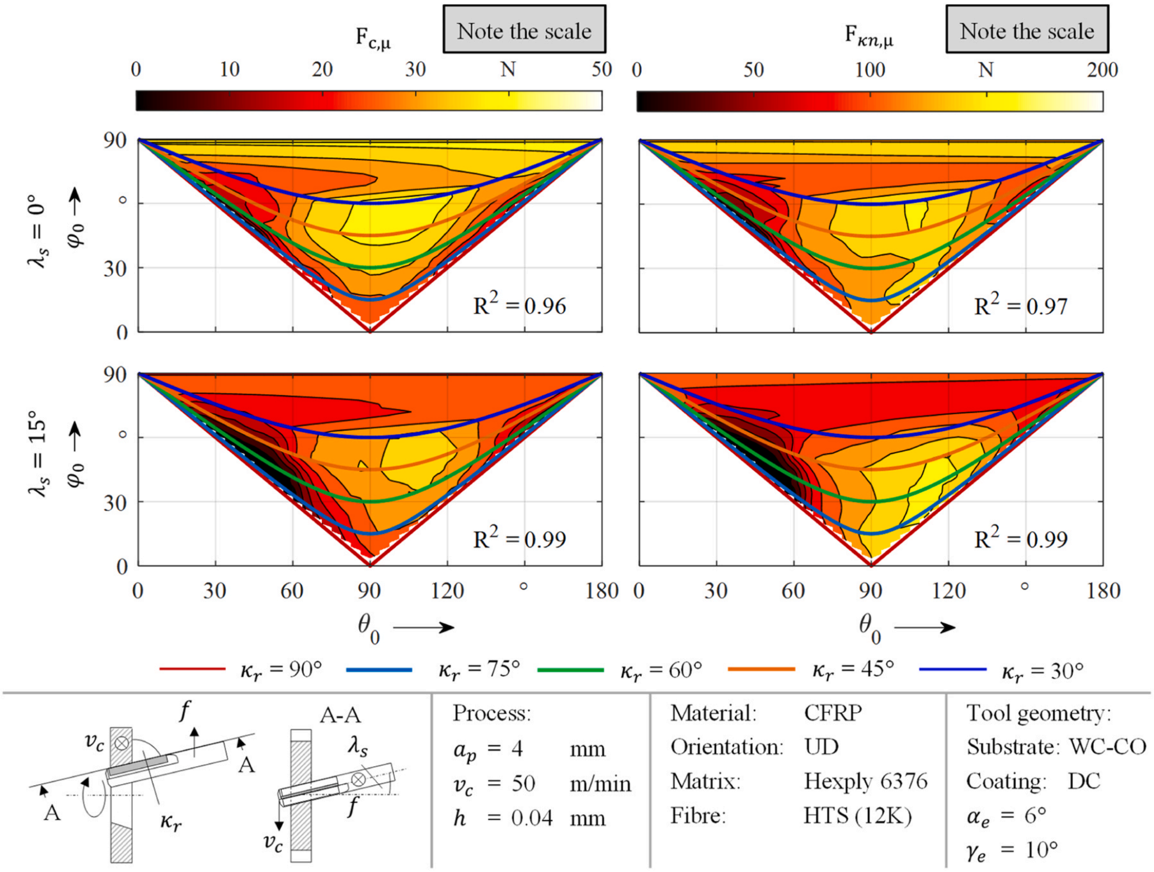

Fig. 12. Results of friction test in the θ_0, φ_0-plane for different λ_s normalised to b_λ= 4 mm.

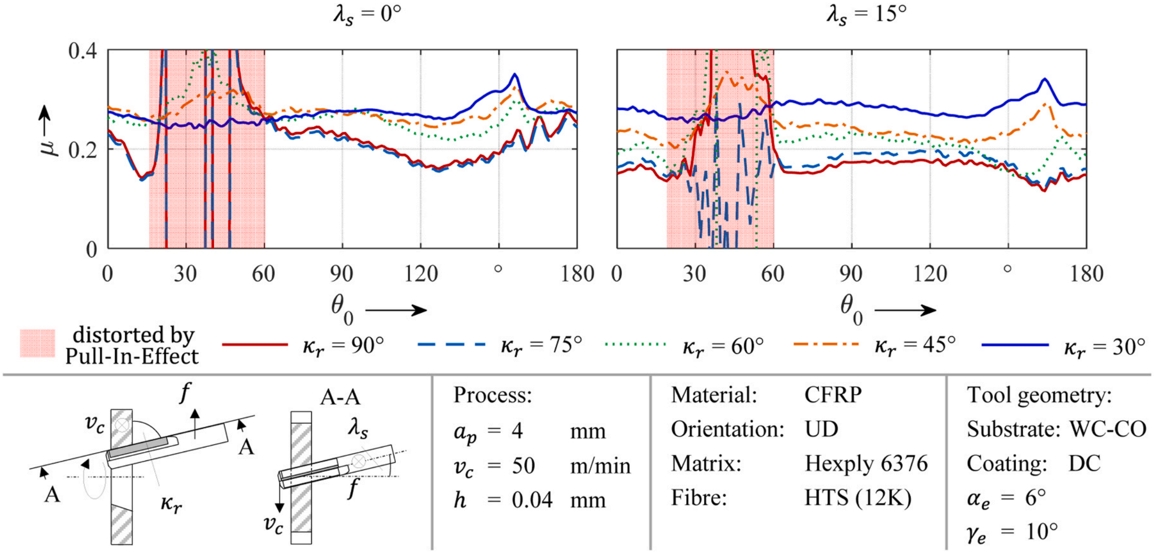

Fig. 13. Friction coefficient as a function of θ_0.

4.3. Friction forces

Friction tests were conducted in order to separate the separation force from the resultant force. To determine the CFRP component of the friction force, the previously experimentally determined aluminium force component during cutting of the aluminium sacrificial ring was subtracted from the friction force during cutting of the aluminium-CFRP stack. The friction force depends on the engaged cutting-edge length b_λ. Using Eq. (8) the friction forces can be normalised to a unit length at $\kappa_r = 90°$ to eliminate the influence of the cutting-edge length. Fig. 11 shows $F_{\kappa n,\mu}$ and $F_{c,\mu}$ as a function of θ_0 normalised to the cutting-edge length $b_\lambda = 4$ mm. $F_{\kappa t,\mu}$ is always close to 0 in the friction tests.

The friction forces $F_{c,\mu}$ and $F_{\kappa n,\mu}$ for $\lambda_s = 15°$ in the θ_0-φ_0-plane are shown in Fig. 12. Compared to the friction forces at $\lambda_s = 0°$, the friction forces decrease with increasing λ_s. Since $F_{\kappa t,\mu}$ is zero for $\lambda_s > 0°$, the friction force is only divided into a tangential $F_{c,\mu}$ and normal $F_{\kappa n,\mu}$

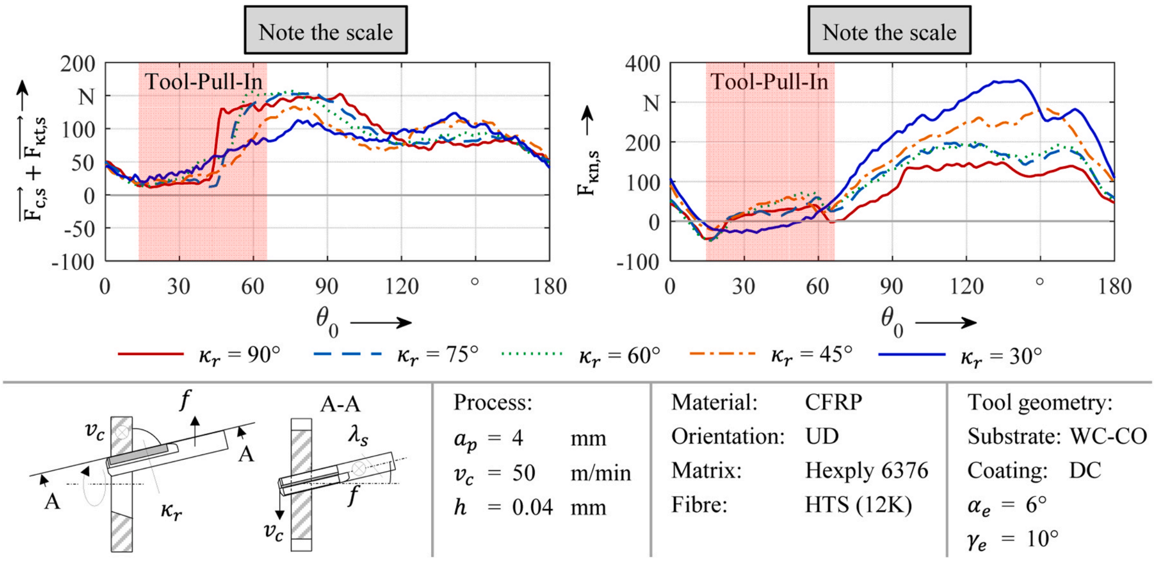

Fig. 14. Separation force components for $\lambda_s = 15°$.

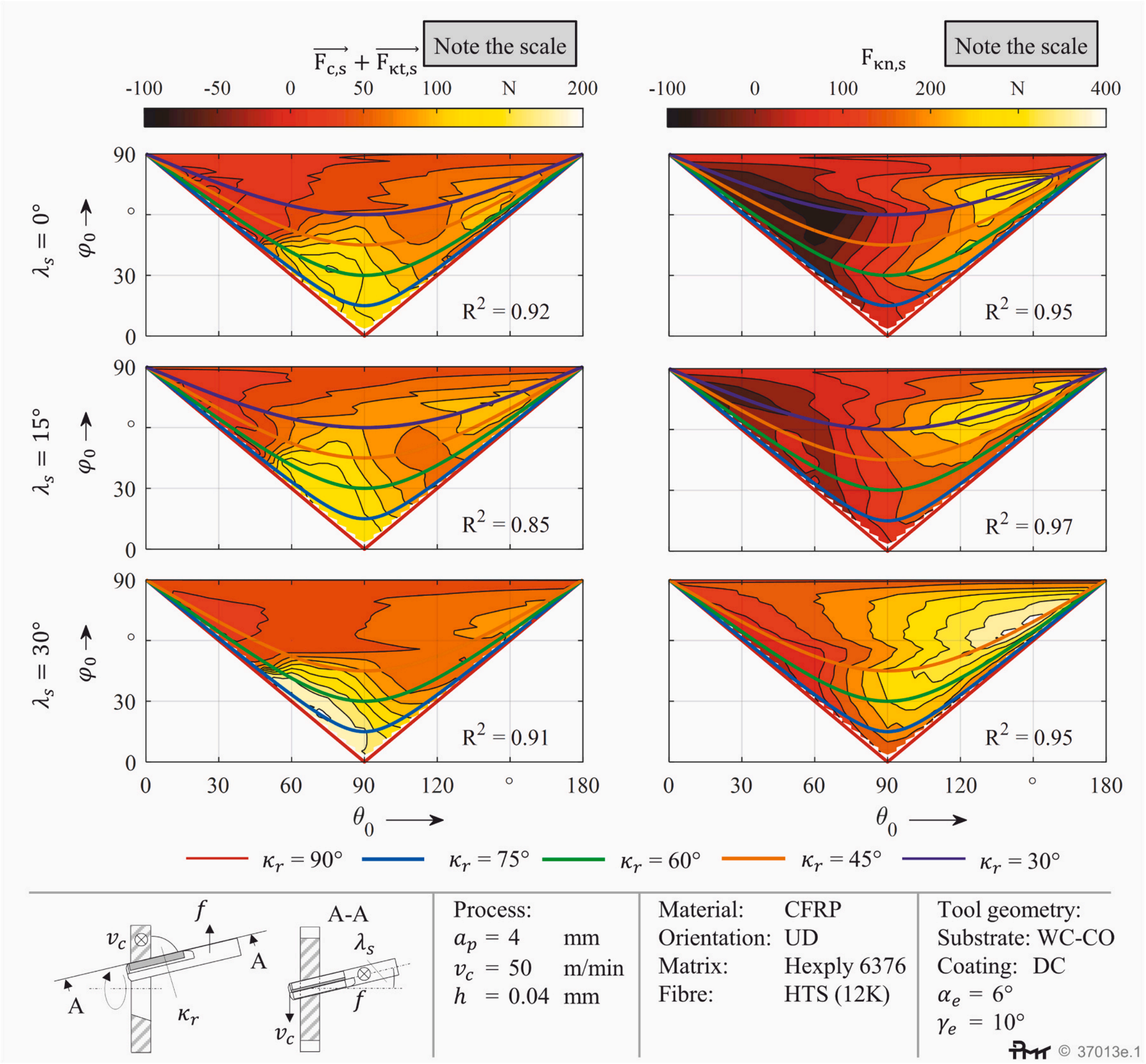

Fig. 15. Separation force components in the θ_0, φ_0-plane for different λ_s normalised to $b_\lambda = 4$ mm.

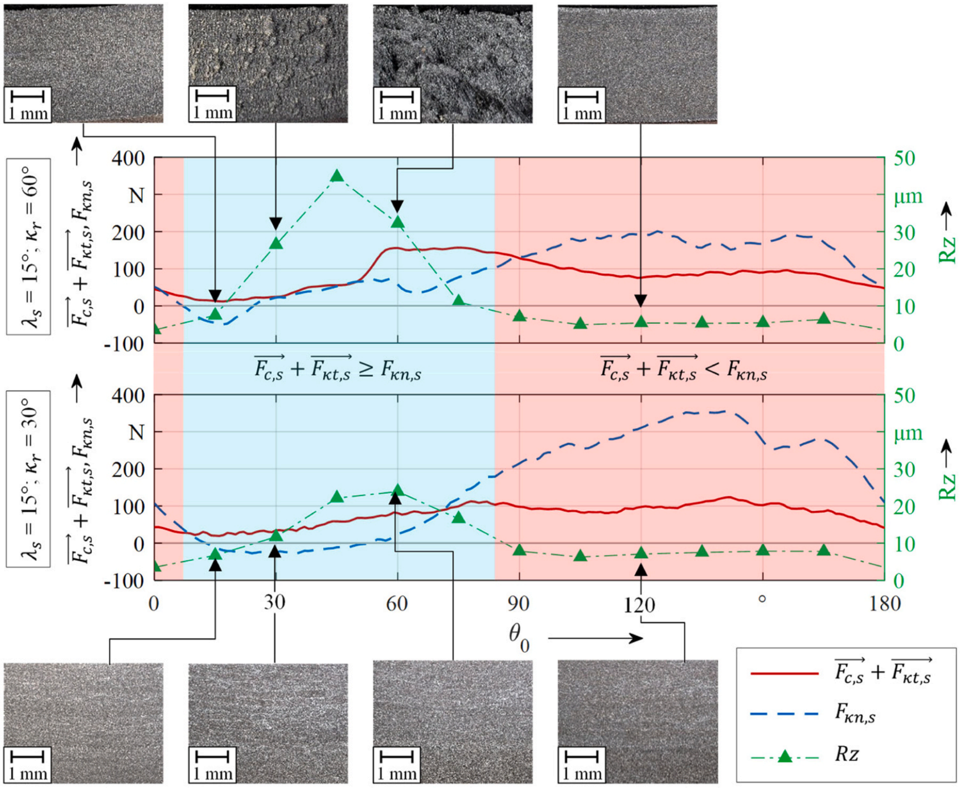

Fig. 16. Comparison of the separation force and the roughness.

component to the cutting direction. The coefficient of friction can be calculated as follows:

$$\mu = \frac{F_{c,\mu}}{F_{\kappa n,\mu}} \tag{17}$$

In the range of 20° $< \theta_0 < 60°$, the measured friction forces for $\kappa_r = 90 – 60°$ are very low. This is due to a excess of the bore hole in this area, which is caused by the tool-pull-in effect, so the cutting edge has no contact with the workpiece. Consequently, results obtained in this range should be cautiously applied when determining the coefficient of friction. This specific zone is visually highlighted on the diagram. Fig. 13 shows the development of μ over θ_0 at different setting angles. μ is in the same magnitude given in previous works [17] at $\kappa_r = 90°$. With decreasing κ_r μ increases from μ = 0.18 at $\kappa_r = 90°$ up to μ = 0.34 at $\kappa_r = 30°$.

4.4. Separation forces

Knowing the friction and process forces for each spatial engagement condition, the separation forces can be calculated. Fig. 14 shows the separation force sum of $\overrightarrow{F_{c,s}} + \overrightarrow{F_{\kappa t,s}}$ for $\lambda_s = 15°$ at different κ_r. Varying engagement conditions lead to different separation forces at the same θ_0.

For the force $F_{\kappa n,s}$ (Fig. 14) perpendicular to the cutting plane, negative forces occur in the range 10° $< \theta <$ 20° for all κ_r. Here the cutting edge seems to dig under the fibres without causing an inter-fibre-failure. Further on, a drop in $F_{\kappa n,s}$ occurs in the range 50° $< \theta <$ 65°. Here, due to the favourable fibre orientation for an inter-fibre failure, numerous cracks propagate into the laminate. Puck et al. identified a favourable fibre cutting angle for inter-fibre failure in the range $\theta_0 = 50$ - 60° [15,16]. Furthermore, the minimum of the forces moves to lower θ_0 with decreasing κ_r. For $\kappa_r = 30°$, negative forces occur in the range 10° $< \theta_0 <$ 55°. Due to the low κ_r, the tool-pull-in effect occurs over a longer contact distance and combines both minima into one.

As the separation force components $\overrightarrow{F_{c,s}} + \overrightarrow{F_{\kappa t,s}}$ and $F_{\kappa n,s}$ are constant for $\theta_0 = 0°$ and 180° in respective of λ_s and κ_r the constraint for the θ_0-φ_0-description is fulfilled, so that these can be represented in the θ_0-φ_0-plane. The sum of forces $\overrightarrow{F_{c,s}} + \overrightarrow{F_{\kappa t,s}}$ (Fig. 15) show the highest values in the area 45° $< \theta_0 <$ 110° and 0° $< \varphi_0 <$ 45° and a further increase of forces in the area 120° $< \theta_0 <$ 160° and 45° $< \varphi_0 <$ 75°. For 0° $< \theta_0 <$ 45° and 45° $< \varphi_0 <$ 90° the forces reach a minimum. At the line $\varphi_0 = \theta_0$ a jump in forces takes place.

In Fig. 15, the force $F_{\kappa n,s}$ perpendicular to the cutting plane is depicted. The highest forces occur in the range 110° $< \theta_0 <$ 180° and 30° $< \varphi_0 <$ 80°. Basically, the contour lines of the contour plot align vertically. No measurement above $\kappa_r = 30°$ was possible. Hence, these values have inaccuracies due to extrapolation. This area shall be investigated with other machining processes in the future. In summary, the friction and separation components of the resultant force show significantly different behaviours depending on the engagement conditions.

$\overrightarrow{F_{c,s}} + \overrightarrow{F_{\kappa t,s}}$ is not affected by the change of λ_s. $F_{\kappa n,s}$ increases with increasing λ_s. By increasing $F_{\kappa n,s}$ tool-pull-in can be prevented with increasing λ_s. However, this does not lead to better surface quality in the investigated λ_s-range.

4.5. Correlation between process forces and surface roughness

Fig. 16 illustrates a comparison of the resultant force components with surface images and the roughness Rz. Two areas are highlighted $\overrightarrow{F_{c,s}} + \overrightarrow{F_{\kappa t,s}} \geq F_{\kappa n,s}$ (10° $< \theta_0 <$ 80°) and $\overrightarrow{F_{c,s}} + \overrightarrow{F_{\kappa t,s}} < F_{\kappa n,s}$. In the first, the tool pull-in effect with increasing inter-fibre failure with increasing θ_0 occurs and the roughness values are high. In the second area, the fibres are separated individually causing a low roughness level and high $F_{\kappa n,s}$. An increase in surface roughness is seen at $\theta_0 = 45°$, coinciding with a steep rise of $\overrightarrow{F_{c,s}} + \overrightarrow{F_{\kappa t,s}}$ and $F_{\kappa n,\mu}$. In the range 50° $< \theta_0 <$ 165°, $F_{\kappa n,s}$ reaches its minimum and also the highest roughness Rz occurs. Thus, the tool pull-in effect is characterised by a drop of $F_{\kappa n,s}$ as well as by an increase of surface roughness. At $\theta_0 = 80^\circ$, $F_{\kappa n,s}$ rises to $\overrightarrow{F_{c,s}} + \overrightarrow{F_{\kappa t,s}} \geq F_{\kappa n}$ again. The roughness decreases and the surface does not show a stepped surface. At $\theta_0 = 120^\circ$ the equation $\overrightarrow{F_{c,s}} + \overrightarrow{F_{\kappa t,s}} < F_{\kappa n,s}$ is fulfilled, the roughness Rz reaches its minimum and the surface is smooth.

5. Summary and outlook

Significant advancements were achieved through comprehensive investigations across the entire range of fibre cutting angles, particularly concerning the exploration of surface roughness, machining forces and friction coefficients for the whole range of the fibre cutting angle θ. With the spatial description of the engagement conditions during machining of CFRP and the proposed decomposition of forces the following results can be stated regarding the experimental setup, the machining forces and the surface roughness.

- For investigations of $\lambda_s > 15^\circ$ the proposed experimental setup is not well suited.
- In the range of $45 < \theta_0 < 75^\circ$ and $45 < \varphi_0 < 15^\circ$ the surface roughness reaches its maximum and decreases with decreasing κ_r.
- The decomposition of the resultant force into the force sum $\overrightarrow{F_c} + \overrightarrow{F_{\kappa t}}$ and $F_{\kappa n}$, as well as the further decomposition into the friction and separation components, proved to be applicable for the description of the engagement conditions during the machining of CFRP with spatial angles (θ_0, φ_0).
- λ_s shows no significant effect on the sum of forces $\overrightarrow{F_c} + \overrightarrow{F_{\kappa t}}$ and $F_{\kappa n}$. Whereas both force components increase with decreasing κ_r.
- The friction coefficient μ increases with increasing κ_r from $\mu = 0.18$ at $\kappa_r = 90^\circ$ to $\mu = 0.34$ at $\kappa_r = 30^\circ$.
- The tool pull-in effect can be characterised by increasing inter-fibre failure with increasing θ_0, resulting in high surface roughness and partly negative $F_{\kappa n,s}$.
- With the proven validity of the process-independent description of engagement conditions for CFRP data obtained in internal transversal turning will be used in the future to model and predict the process forces and surface roughness of more complex machining processes like milling which is widely used in industrial applications.

For the investigation of still unknown engagement conditions in the θ_0-φ_0-plane and higher λ_s, experiments with linear machining processes are necessary. Since friction and separation forces can be represented in the θ_0-φ_0-plane, the development of a CFRP dedicated force model which takes θ_0 and φ_0 will be possible in the future.

Declaration of Competing Interest

The authors declare that they have no known competing financial interests or personal relationships that could have appeared to influence the work reported in this paper.

Acknowledgments

The authors gratefully acknowledge the financial support of the German Research Foundation, Deutsche Forschungsgemeinschaft (DFG) within the research project HI 843/13-1, project number 457264004.

References

[1] Sauer M., Schüppel D. - Market Report 2022- The global Market for carbon fibers and carbon composites – Market Developments, Trends, Forecasts and Challenges – freely accessible short version. Composites United e.V., 2023.

[2] Soo-Jin Perk, Carbon Fibers – Second Edition, Springer Series in Materials Science Volume 210, (2018), https://doi.org/10.1007/978–981-13–0538-2.

[3] Schütte C., Bohren und Hobeln von kohlenstofffaserverstärkten Kunststoffen unter besonderer Berücksichtigung der Schneide-Faser-Lage. Dissertation. Technische Universität Hamburg-Harburg, Hamburg, 2014.

[4] Hintze W, Clausen R, Schütte C, Kroll K. Evaluation of the total cutting force in drilling of CFRP: a novel experimental method for the analysis of the cutting mechanism. Prod Eng 2018;12:431–40. https://doi.org/10.1007/s11740-018-0807-2.

[5] Voß R.: Fundamentals of carbon fibre reinforced polymer (CFRP) machining. Dissertation.ETH Zürich, Zürich, 2017.

[6] Hintze W, Hartmann D, Schutte C. Occurrence and propagation of delamination during the machining of carbon fibre reinforced plastics (CFRPs)—an experimental study. Compos Sci Technol 2011;71(15):1719–26.

[7] Karpat Y, Bahtiyar O, Değer B. Mechanistic force modeling for milling of unidirectional carbon fiber reinforced polymer laminates. Int J Mach Tools Manuf 2012;56:79–93. https://doi.org/10.1016/j.ijmachtools.2012.01.001.

[8] Jawahir I, Brinksmeier E, M'Saoubi R, Aspinwall D, Outeiro J, Meyer D, Umbrello D, Jayal A. Surface integrity in material removal processes: recent advances. CIRP Ann 2011;60(2):603–26. https://doi.org/10.1016/j.cirp.2011.05.002.

[9] Hintze W, Clausen R, Schütte C, Kroll K. Evaluation of the total cutting force in drilling of CFRP - a novel experimental method for the analysis of the cutting mechanism. Prod Eng 2018;2018:S. 1–10.

[10] Calzada KA, Kapoor SG, DeVor RE, Samuel J, Srivastava K. Modeling and interpretation of fiber orientation-based failure mechanisms in machining of carbon fiber-reinforced polymer composites. J Manuf Process 2012;14:141–9. https://doi.org/10.1016/j.jmapro.2011.09.005.

[11] Hintze W, Brouschkin A, Köttner L, Bluehm M. Model based prediction of force and roughness extrema inherent in machining of fibre reinforced plastics using data merging. In: Liewald M, Verl A, Bauernhansl T, Möhring H-C, editors. Production at the Leading Edge of Technology, Proceedings of the 12th Congress of the German Academic Association for Production Technology (WGP), University of Stuttgart, October 2022. Springer Verlag Berlin; 2022. https://doi.org/10.1007/978-3-031-18318-8_5.

[12] Chen L, Zhang K, Cheng H, Qi Z, Meng Q. A cutting force prediction model in orthogonal machining of unidirectional CFRP for entire range of fibre orientation. Int J Adv Manuf Technol 2017;89:833–46. https://doi.org/10.1007/s00170-016-9059-5.

[13] Sung N-H, Suh NP. Effect of fiber orientation on friction and wear of fiber reinforced polymeric composites. Wear 1979;53:129–41. https://doi.org/10.1016/0043-1648(79)90224-2.

[14] Hintze W., CFK-Bearbeitung- Technologien für Faserverbundkunststoffe und den hybriden Leichtbau., Springer-Verlag GmbH Deutschland, 2021, ISBN 978–3-662–63265-9, https://doi.org/10.1007/978–3-662–63265-9.

[15] Puck A, Schürmann H. Failure analysis of FRP laminates by means of physically based phenomenolical models (September–October) Compos Sci Technol 2002;62 (12–13):1633–62. https://doi.org/10.1016/S0266-3538(01)00208-1.

[16] Schürmann H. Page 416, ISBN 978-3-540-72189-5. Konstruieren mit Faser-Kunststoff-Verbunden. 2nd Volume. Springer Berlin Heidelberg New York; 2007. https://doi.org/10.1007/978-3-540-72190-1.

[17] Voss R, Seeholzer L, Kuster F, Wegener K. Cutting process tribometer experiments for evaluation of friction coefficient close to a CFRP machining operation. Procedia CIRP 2017;66:204–9. https://doi.org/10.1016/j.procir.2017.03.225.